Energy Materials

Article

Constructing stable lithium metal anodes using a lithium adsorbent with a high Mn³⁺/Mn⁴⁺ ratio

Yue Zhao[1], Ziqiang Liu[1,2], Zhendong Li[1], Zhe Peng[1,*], Xiayin Yao[1,*]

[1]Ningbo Institute of Materials Technology and Engineering, Chinese Academy of Sciences, Ningbo 315201, Zhejiang, China.
[2]Center of Materials Science and Optoelectronics Engineering, University of Chinese Academy of Sciences, Beijing 100049, China.

*Correspondence to: Prof. Zhe Peng, Ningbo Institute of Materials Technology and Engineering, Chinese Academy of Sciences, 1219 West Zhongguan Road, Ningbo 315201, Zhejiang, China. E-mail: pengzhe@nimte.ac.cn; Prof. Xiayin Yao, Ningbo Institute of Materials Technology and Engineering, Chinese Academy of Sciences, 1219 West Zhongguan Road, Ningbo 315201, Zhejiang, China. E-mail: yaoxy@nimte.ac.cn

Abstract

Lithium (Li) metal batteries (LMBs) have emerged as the most prospective candidates for post-Li-ion batteries. However, the practical deployment of LMBs is frustrated by the notorious Li dendrite growth on hostless Li metal anodes. Herein, a protonated Li manganese (Mn) oxide with a high Mn^{3+}/Mn^{4+} ratio is used as a Li adsorbent for constructing highly stable Li metal anodes. In addition to the Mn^{3+} sites with high Li affinity that afford an ultralow Li nucleation overpotential, the decrease in the average Mn^{n+} oxidation state also induces a disordered adsorbent structure via the Jahn-Teller effect, resulting in improved Li transfer kinetics with a significantly reduced Li electroplating overpotential. Based on the mutually improved Li diffusion and adsorption kinetics, the Li adsorbent is used as a versatile host to enable dendrite-free and stable Li metal anodes in LMBs. Consequently, a modified $Li||LiNi_{0.8}Mn_{0.1}Co_{0.1}O_2$ (NMC811) coin cell with a high NMC811 loading of 4.3 mAh cm^{-2} delivers a high Coulombic efficiency of 99.85% over 200 cycles and the modified Li||NMC811 pouch cell also achieves a remarkable improvement in electrochemical performance. This work demonstrates a novel approach for the preparation of highly efficient Li protection structures for safe LMBs with long lifespans.

Keywords: Lithium metal batteries, lithium metal anodes, dendrites, protonated lithium manganese oxide

INTRODUCTION

Over the past three decades, lithium (Li)-ion batteries (LIBs) have significantly impacted modern society and catalyzed the fast growth of energy-storage markets[1]. Accordingly, safer batteries with higher energy density are urgently required, especially for electric vehicle manufacturing, where a high energy density of 500 Wh kg^{-1} is desired, which unfortunately exceeds the upper limit of LIBs[2]. Hence, developing next-generation high-energy batteries is being widely investigated at present. The Li metal anode, possessing an ultrahigh capacity (3860 mAh g^{-1}) and the lowest redox potential (-3.04 V *vs.* a standard hydrogen electrode), is a key component for building satisfactory Li metal battery (LMB) systems[3]. However, achieving a practical rechargeable LMB is still plagued by the poor cycling stability of the Li metal anode, where the irregular Li dendrites associated with Li electroplating can cause severe safety hazards, such as internal shorting and thermal runaway[4]. Furthermore, the native and weak solid electrolyte interphase (SEI) on the Li metal anode is not able to withstand repeated Li plating/stripping, resulting in continuous crack/reformation cycles that dramatically lower the Coulombic efficiency (CE) of Li metal cycling[4]. In addition, the dendrite growth is accelerated under high current density[5], implying that LMB failure will be aggravated in practical cell configurations, where the large electrode surfaces with high active material loading impose a generally high current output, even at moderate charge/discharge rates.

Hence, stabilizing the Li metal anode is a prerequisite for the development of LMBs, where significant progress has been made by reinforcing Li/electrolyte interfaces through electrolyte designs and constructing artificial protective layers[6-9]. Furthermore, interfacial reinforcement to guide Li plating in a uniform manner is also important in promoting the deployment of the Li metal anode in LMBs. The latter has been achieved by using substrates with high Li affinity based on metal oxides that generate a lithiophilic Li_2O matrix following the conversion reaction of $M_xO + 2Li^+ + 2e^- \rightarrow xM + Li_2O$[10-12] or Li alloys that possess a high solid solubility with Li to lower the nucleation barrier of Li electrodeposits[13-15]. Despite these achievements, the low initial CEs caused by the conversion reaction of the metal oxides or the structural pulverization of the Li alloys still remain concerns for practical applications. Alternatively, other approaches to generate phase-change-free lithiophilic interfaces, including nitrogen- or fluorine-doped carbon[16,17] and faceted copper (Cu) surfaces[18,19], have been investigated to enable the stable cycling of Li anodes at current densities up to 4 mA cm^{-2} in coin cells. All these studies demonstrate that the rational design of lithiophilic materials can be a formidable challenge for advancing the practical use of structured or hosted Li metal anodes in LMBs.

Recently, we demonstrated an underpotential deposition (UPD) process of Li atoms on manganese (Mn)-based substrates[20]. The UPD can guide few-layer and uniform Li atom adsorption on the substrates, resulting in highly compact and dendrite-free Li electroplating during the subsequent cycling. Inspired by this particular remedy, an in-depth design of a novel lithiophilic host is carried out in this contribution, where a Li adsorbent consisting of protonated Li manganese oxide (LMO) backbone is successively fabricated. Furthermore, it is shown that the Li protection ability of the Li adsorbent depends on the Mn^{3+}/Mn^{4+} ratio of the backbones and a high Mn^{3+}/Mn^{4+} ratio can promote stronger Li adsorbing ability, higher Li deposition uniformity and better Li cycling stability, owing to the Mn^{3+} sites with high Li affinity and the enhanced Li diffusivity in the Jahn-Teller effect-induced disordered structure [Figure 1A]. These results provide novel guidelines for designing highly efficient Li protection structures. Consistently, significantly improved performances of coin and pouch LMBs are demonstrated by using the optimal Li adsorbent as a protective structure for Li metal anodes.

EXPERIMENTAL

Material preparations

MnO_2, lithium hydroxide (LiOH) and N-methyl-2-pyrolidone (NMP) were purchased from Aladdin. Hydrochloric acid (HCl) was purchased from Sinopharm Chemical Reagent Co., Ltd. All chemicals were used without further purification. To prepare the LMOs, uniform mixtures of MnO_2 and LiOH with a certain mass ratio (3:1, 5:1 and 7:1) were heated at 900 °C for 2 h with a ramping rate of 5 °C min^{-1} under air. After cooling to room temperature, the obtained powders were treated with 1.5 M HCl for 12 h. After washing with deionized water several times and drying at 80 °C for 24 h, the final powders were obtained (denoted at HMO-3, HMO-5 and HMO-7, respectively).

The HMO-coated Cu electrodes or separators were prepared by a blade-coating method. The 80 wt.% HMO powders, 10 wt.% conductive carbon black (Super P) and 10 wt.% PVDF binder were dissolved in NMP to obtain a slurry, which was coated on the commercial separator (Celgard 2325, thickness of 25 μm) or Cu foil, followed by drying at 60 °C for 12 h.

Characterization

The microscopy and elemental distribution analyzes were carried out using scanning electron microscopy (SEM, Hitachi S-4800). X-ray diffraction (XRD, Bruker D8 Advance) was performed at 40 kV and 40 mA with Cu-Kα radiation. The surface composition and chemical bond properties were determined using X-ray photoelectron spectroscopy (XPS, Axis Ultra DLD, Kratos). The Brunauer-Emmett-Teller (BET) surface area and average pore diameter were determined by nitrogen adsorption-desorption analysis (Micromeritics ASAP 2020HD88). Raman spectra were obtained with a Raman spectrometer (Renishaw inVia-reflex).

Electrochemical tests

Lithium hexafluorophosphate ($LiPF_6$), ethyl methyl carbonate (EMC), dimethyl carbonate (DMC) and fluoroethylene carbonate (FEC) purchased from Aladdin. All the electrochemical tests carried out in this work used a carbonate electrolyte of 1 M $LiPF_6$ in EMC:DMC:FEC (7:2:1 by vol.). The cyclic voltammetry (CV), electrochemical impedance spectroscopy (EIS) and long-term Li cycling CE tests were carried out in CR2032 coin cells, where bare Cu or HMO-coated Cu (diameter of 13 mm) was used as the working electrode and Li foil (diameter of 10 mm and thickness of 200 μm) was used as both the counter and reference electrodes. An electrolyte amount of 80 μL was introduced to each coin cell. The CV and EIS measurements were performed on a multi-channel electrochemical workstation (Solartron 1470E). The CV curves were recorded in a potential range of -0.5-1 V *vs*. Li/Li$^+$ at 10 mV s^{-1}. The EIS spectra were measured in a frequency range of $0.1\text{-}10^6$ Hz with a voltage perturbation of 10 mV. For long-term cycling test of the Li anode, the desired Li amount was plated on the working electrodes with a selected current density, followed by a stripping process up to a cut-off potential of 1 V *vs*. Li/Li$^+$. The long-term cycling of Li||Cu half cells was performed using LAND CT2001A battery testers.

For the assessment of the full cell performance, coin and pouch Li||$LiNi_{0.8}Mn_{0.1}Co_{0.1}O_2$ (NMC811) cells were assembled. For the Li||NMC811 coin cells, the Li anode (diameter of 15.5 mm and thickness of 600 μm) and NMC811 cathode (diameter of 10 mm and areal loading of ~4.3 mAh cm^{-2}, corresponding to ~205 mAh g^{-1} of active material) were used and separated by the bare or HMO-coated separators (diameter of 19 mm, the HMO coating layer was in contact with the Li anode). The Li||NMC811 coin cells were pre-cycled for three cycles at charge/discharge rates of 0.1 C/0.1 C in a voltage window of 3.0-4.2 V *vs* Li/Li$^+$, followed by cycling at 0.64 C/0.64 C, using LAND CT2001A battery testers. The Li||NMC811 pouch cells were assembled under an argon atmosphere. The 35 mm × 55 mm Li anode (thickness of 50 μm), 30 mm × 50 mm NCM811 cathode (capacity of ~65 mAh) and 40 mm × 60 mm separator (with/without HMO coating layer) were assembled in the pouch cell, in which 1 mL of electrolyte was injected. The Li||NMC811 pouch cells were cycled at charge/discharge rates of 0.1 C/0.1 C in the voltage range of 3.0-4.25 V *vs*. Li/Li$^+$ using Neware battery testers.
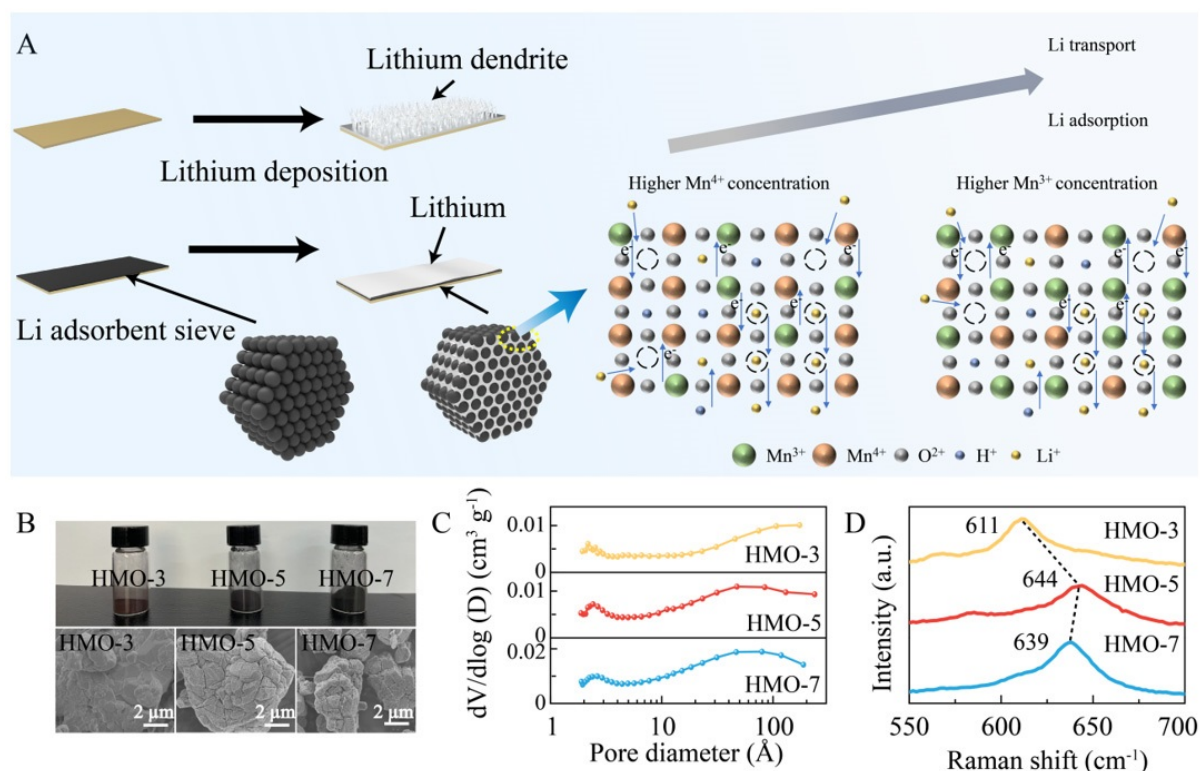
Figure 1. (A) Schematic representation of improved Li electroplating uniformity in Li adsorbent with tuned Mn^{3+}/Mn^{4+} valence states; (B) morphologies; (C) pore distributions; and (D) Raman spectra of prepared HMOs.

RESULTS AND DISCUSSION

The morphologies of HMO-3, -5 and -7 are shown in Figure 1B, with a more compact structure observed for HMO-3, indicating that the LiOH amount implemented in the preparation of LMO can affect the structure of the derived HMO. Consistently, the lowest BET surface area and porosity also belong to HMO-3 [Figure 1C and Supplementary Figure 1]. Interestingly, different from the monotonic evolution of the BET surface area from HMO-3 to -7, an inflection point is observed for the peak shift of the symmetric Mn-O stretching vibration in their Raman spectra [Figure 1D]. Compared to the peak at 630 cm^{-1} for the pristine MnO_2 powders [Supplementary Figure 2][21,22], a continuous peak upshift to 639 and 644 cm^{-1} is observed for HMO-7 and -5, respectively. The latter is a typical Raman response to the Jahn-Teller effect induced by the decrease in the average oxidation state of Mn^{n+}[21,22], indicating the appearance of Mn^{n+} sites ($n < 4$) after protonating the LMO powders. However, a peak downshift to 611 cm^{-1} is observed for HMO-3, indicating the existence of an over-lithiation effect of LMO that undergoes a secondary structural change of the derived HMO. These results demonstrate that the lithiation degree of LMO (depending on the LiOH amount implemented in the preparation) can have a significant effect on the average valence state of Mn^{n+} in the protonated adsorbent structure.

The valence states of HMOs were further quantified by XPS. As shown in the Mn 2p spectra [Figure 2A], both the Mn $2p_{3/2}$ and Mn $2p_{1/2}$ peaks split into Mn^{3+} and Mn^{4+} sub-peaks. The revealed Mn^{3+}/Mn^{4+} peak ratios for HMO-3, -5 and -7 are 0.21, 0.68 and 0.11, respectively. The highest Mn^{3+}/Mn^{4+} peak ratio for HMO-5 is consistent with the inflection point of the Raman shift in Figure 1D. XRD patterns were collected to understand the valence state changes from HMO-3 to -7. It is reported that the XRD patterns between the LMO and the as-protonated HMO are quasi-invariant[23]. As shown in Figure 2B, all the HMO samples
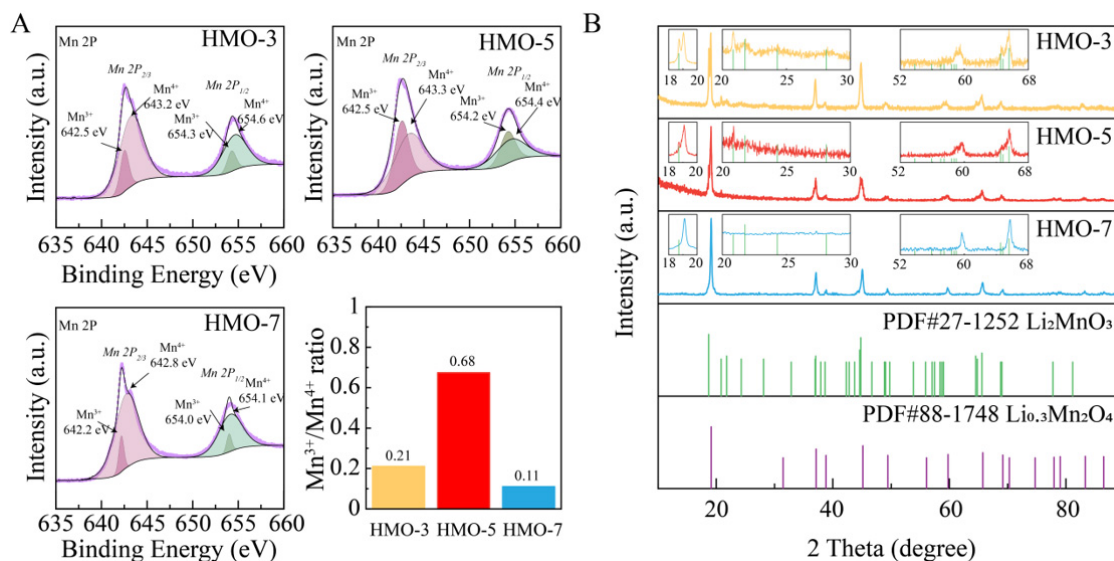
Figure 2. (A) Mn 2p spectra with related Mn^{3+}/Mn^{4+} peak ratio and (B) XRD patterns of prepared HMOs.

exhibit dominant peaks of the spinel structure corresponding to $Li_{0.3}Mn_2O_4$, which represents the main substance of the LMO prepared in this work. However, for HMO-3, additional peaks corresponding to Li_2MnO_3 are observed. The presence of Li_2MnO_3 in HMO-3 is probably due to the excessive LiOH amount implemented in the preparation of LMO, where two stoichiometric lithiation processes with Li:Mn ratios of 0.15:1 and 2:1 coexist, leading to the formation of $Li_{0.3}Mn_2O_4$ and Li_2MnO_3, respectively. It is noteworthy that trace signals of Li_2MnO_3 are also observed in the XRD pattern of HMO-5, suggesting that the concentration of the protonated $Li_{0.3}Mn_2O_4$ achieves nearly the maximum value and a further increase in LiOH amount during the preparation of LMO will only engender the formation of Li_2MnO_3 with Mn^{4+} sites (as for HMO-3). Thus, these results depict the existence of an optimal MnO_2:LiOH stoichiometry during the LMO preparation, leading to the highest Mn^{3+}/Mn^{4+} ratio of the derived HMO (this optimal ratio is estimated to be 5:1 for the preparation of HMO-5).

Generally, the decrease in the average oxidation state of Mn^{n+} can induce the Jahn-Teller effect that leads to the disordered structure of LMO with reduced Li storage capability[24]. However, Jahn-Teller-assisted sodium (Na) diffusion for high-performance Na-ion batteries has also been reported, reflecting another aspect of the Jahn-Teller deformation for increasing the ion mobility in the Mn oxide-based host[25]. In our previous work, the Mn-based substrate showed an excellent ability for Li adsorption[20]. Hence, a synergy between the Li transfer and adsorption kinetics is expected to affect Li plating/stripping in the HMOs with the tuned Mn^{3+}/Mn^{4+} ratio.

The study of Li plating/stripping kinetics on the investigated substrates was carried out through electrochemical approaches, where the powders of HMOs were coated on Cu foils to form the working electrodes [Supplementary Figure 3]. The voltage profiles of the initial Li electroplating were first assessed, where the Li nucleation overpotential can be revealed as the difference between the voltage dip and plateau[26]. At a current density of 1 mA cm^{-2}, a high Li nucleation overpotential of ~180 mV was achieved on bare Cu, which can result in unevenly distributed Li nuclei, followed by dendrite growth [Figure 3A]. In sharp contrast, an ultralow Li nucleation overpotential of ~10 mV was obtained for the HMO-coated Cu electrodes, demonstrating the high Li affinity of the Mn-based substrates[20]. However, the voltage plateaus of Li electroplating are different among the HMO-coated Cu electrodes, with values of 44, 33 and 65 mV for
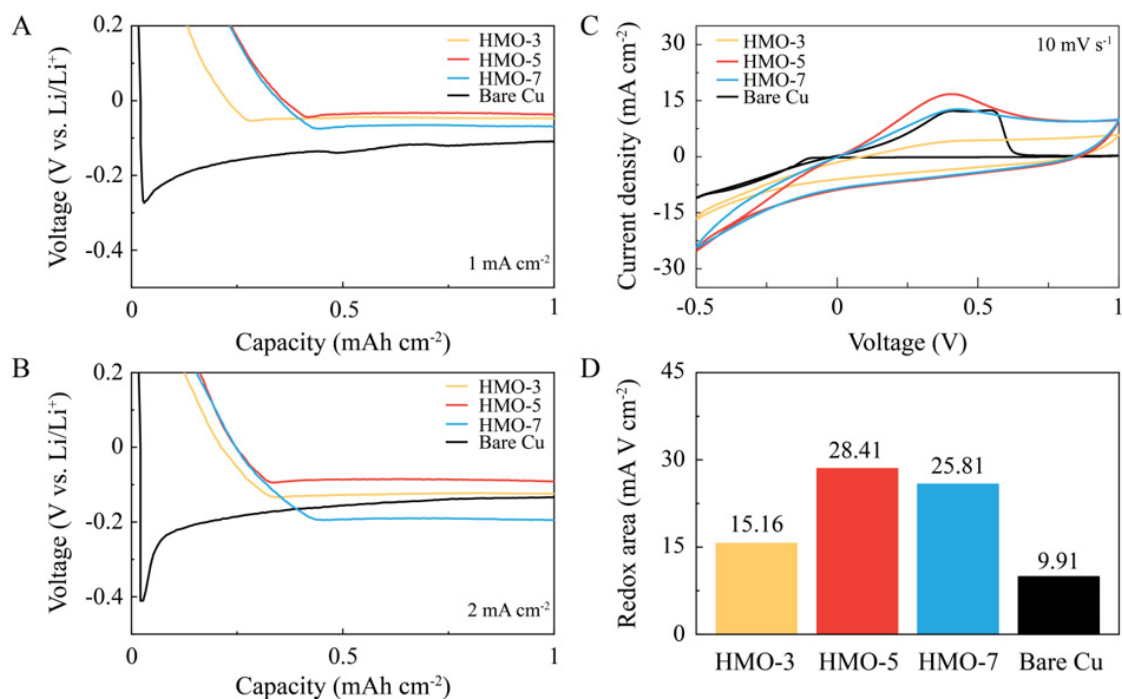
Figure 3. Voltage profiles of initial Li electroplating on investigated substrates at (A) 1 and (B) 2 mA cm^{-2}. (C) CV curves with (D) related redox areas for Li plating/stripping on investigated substrates.

HMO-3, -5 and -7, respectively. These results demonstrate the improved Li diffusivity with the increased Mn^{3+}/Mn^{4+} ratio of the Li adsorbent. At a higher current density of 2 mA cm^{-2}, the same phenomena are observed, where a further enlarged Li nucleation overpotential of ~287 mV was achieved on bare Cu. However, the ultralow Li nucleation overpotential of ~10 mV was maintained for the HMO-coated Cu electrodes [Figure 3B]. It is noteworthy that the differences in the Li plating plateaus were enlarged among the HMO-coated Cu electrodes at the higher current density, with values of 122, 85 and 190 mV for HMO-3, -5 and -7, respectively. Thus, it is demonstrated that increasing the Mn^{3+}/Mn^{4+} ratio can be an effective approach to boost the Li transfer kinetics in the Mn oxide-based Li host.

In addition to Li diffusion, Li adsorption is another important factor that affects the functionality of the host structure. Thus, the interfacial behavior during Li plating/stripping was also studied by CV tests at a voltage range of -0.5-1 V *vs.* Li/Li$^+$ [Figure 3C]. For bare Cu, posterior to the cathodic scanning corresponding to metallic Li plating, the anodic peak rapidly vanished beyond 0.5 V, reflecting the completion of a typical faradaic Li plating/stripping process. In contrast, all the HMO-coated Cu electrodes exhibit capacitive-adsorption featured curves with supplementary redox areas extended to 1 V, demonstrating the effective Li adsorption on the Mn-based substrates. Furthermore, the redox area of HMO-3 is lower than those of HMO-5 and -7 [Figure 3D]. This reflects the ion sieving effect related to the pore size of the adsorbent[27], where the more compact structure of HMO-3 [Figure 1B and C and Supplementary Figure 1], probably arising from the co-produced Li$_2$MnO$_3$ phase [Figure 2B], leads to the reduced Li adsorbing ability. Hence, it can be deduced that the Li adsorbing ability of HMOs mainly arises from the protonated Li$_{0.3}$Mn$_2$O$_4$ phase. The largest redox area belongs to HMO-5 despite it having a lower BET surface area than that of HMO-7, indicating that the pore structure is not the only factor in determining the Li adsorption ability. The higher Mn^{3+}/Mn^{4+} ratio represents a more dominant factor, owing to the higher Li affinity of Mn^{3+} sites compared with the Mn^{4+} counterparts.

The Li electroplating behavior in the HMOs was further studied by SEM. To provide a global perspective of Li deposition in the host structure of the HMOs, cross-sectional SEM images were obtained for the HMO-coated separators. As shown in Figure 4A, for a Li electroplating amount of 2 mAh cm^{-2}, a tight HMO/separator interface without any cracks/detachments is observed for HMO-5, indicating the uniform storage of deposited Li in the Li adsorbent. It is noteworthy that some Li deposits are observed on the other side of the HMO-5 layer, which represents the HMO/Cu interface in the operating cell. This underneath deposition feature indicates the Li diffusion throughout the whole HMO-5 layer. With an increasing Li electroplating amount to 4 mAh cm^{-2}, the HMO/separator interface still remains intact, demonstrating the good ability of the HMO-5 layer to accommodate high-capacity Li deposition. Similar features are also observed for HMO-3 and -7 [Supplementary Figure 4A and B, respectively]. These results demonstrate the general ability of the Mn-based structures to guide uniform Li deposition. However, as shown by the SEM images of the bottom side of the HMO-coated separators after Li electroplating of 4 mAh cm^{-2}, dendritic deposits are observed for the HMO-3-coated separator [Supplementary Figure 5A], while locally accumulated deposits are found for the HMO-7-coated separator [Supplementary Figure 5C].

In contrast, a dendrite-free and uniform surface is observed for the HMO-5-coated separator [Supplementary Figure 5B], reflecting the ordered deposition of Li in the HMO-5 based host. Furthermore, as shown by the top-view SEM images of Li deposits on the HMO-coated Cu electrodes [Figure 4B and Supplementary Figure 6], with increasing Li plating capacity, larger and more compact Li flacks are formed on the HMO-5 layer, compared with those on HMO-3 and -7. This indicates a more uniform Li electroplating feature induced by the mutually boosted Li diffusion and adsorption kinetics because of the high Mn^{3+}/Mn^{4+} ratio. The latter is expected to minimize the surface area contact of the deposited Li with the electrolyte and alleviate the mechanical strain on the SEI layer, thus affording higher and stable Li cycling CE.

The Li cycling CEs were assessed in Li||Cu half cells, where the bare and HMO-coated Cu electrodes were compared. As shown in Figure 5A, under 1 mA cm^{-2} and 1 mAh cm^{-2}, the HMO-coated Cu exhibits much better Li cycling stability than that of bare Cu, demonstrating the ability of the Mn-based substrates for Li protection. Notably, a long and stable cycling over nearly 600 cycles was achieved by the cell using the HMO-5-coated Cu, exhibiting the best performance among the HMO-coated Cu electrodes. In addition, the average Li CE in the HMO-5-coated Cu is ~96.1%, which is higher than ~95.0% and ~95.3% in the HMO-3 and HMO-7-coated Cu, respectively. EIS measurements were also carried out to reveal the interfacial impedances of the investigated electrodes upon cycling. As shown in Supplementary Figure 7, the smallest semi-circle reflecting the lowest interfacial impedance always belongs to the HMO-5-coated Cu at various cycling states, demonstrating the excellent ability of the HMO-5 layer to suppress side reactions between Li and the electrolyte. By further raising the current density and/or capacity of the cycling conditions, such as 1 mA cm^{-2} and 2 mAh cm^{-2} [Figure 5B] and 2 mA cm^{-2} and 2 mAh cm^{-2} [Figure 5C], the HMO-5-coated Cu still exhibits the best Li cycling stability among the investigated samples.

The outstanding Li protection ability of the HMO-5-coated Cu confirms the importance of tuning the Mn^{3+}/Mn^{4+} ratio for improved Li diffusion and adsorption kinetics in the Li adsorbent. Generally, compared with other hazardous issues, such as dendrite-triggered internal shorting or thermal runaway, high impedance-induced voltage shutdown is the most encountered cause of LMB failure. This is mainly due to the fast accumulation of highly impeding side products on the anode surface, arising from the reactions of fresh Li and electrolyte at the cracked SEI zones. The high Li electroplating uniformity on the HMO-5-coated Cu can result in minimized SEI cracks and suppressed side reactions. As shown in Supplementary Figures 8 and 9, instead of dendritic/mossy side products accumulated on the cycled bare
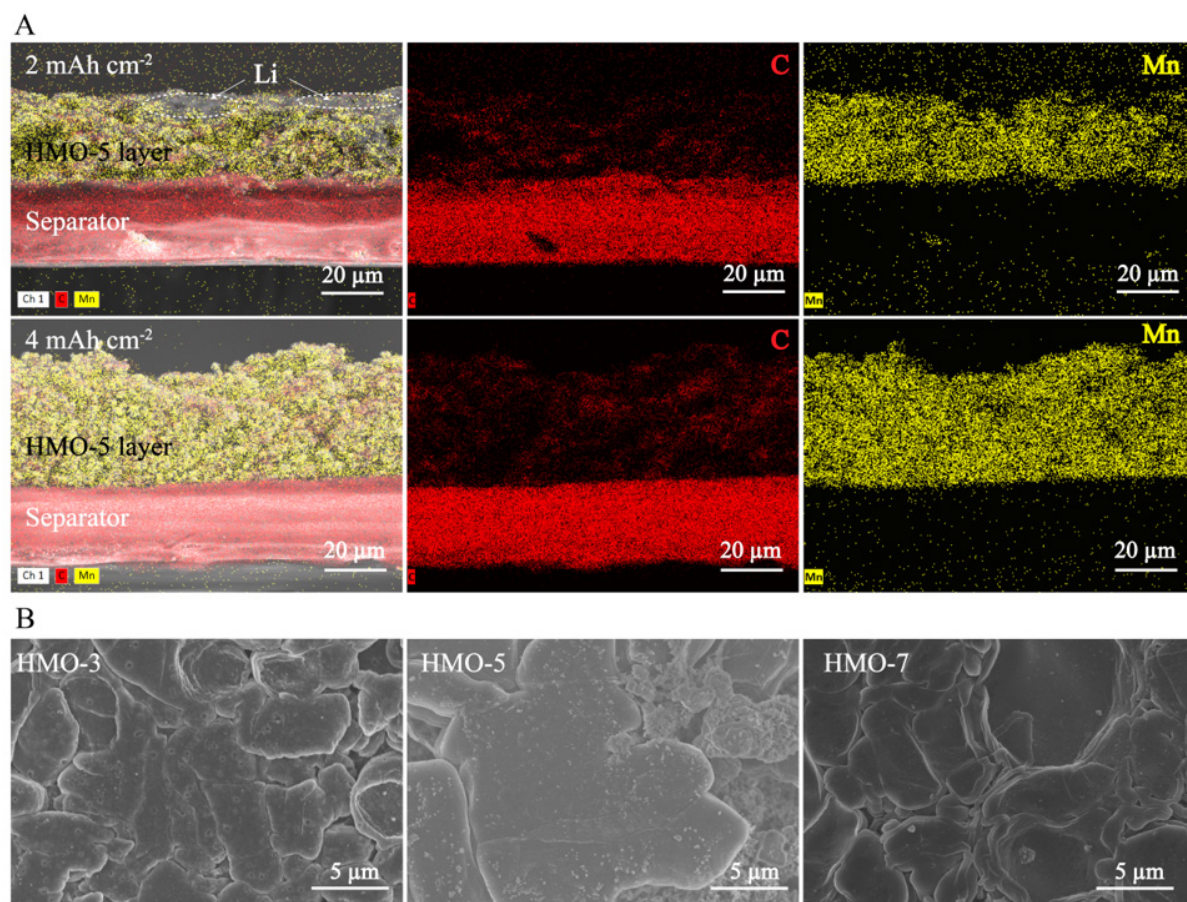
Figure 4. (A) Cross-sectional SEM images of HMO-5-coated separator after Li electroplating of 2 and 4 mAh cm^{-2}. (B) top-view SEM images of Li deposits on HMO-coated-Cu electrodes after Li electroplating of 4 mAh cm^{-2}.

Cu and HMO-3-coated Cu after 50 and 100 cycles, more compact surfaces are observed on the HMO-5 and HMO-7-coated Cu with a stronger Li adsorption ability. In particular, the dendrite-free-featured surface was maintained on the HMO-5-coated Cu in prolonged cycling. It is noteworthy that the Li surface morphology and the electrochemical stability are highly correlated. The Li‖Li symmetrical cell system was employed to study the voltage profile of Li plating/stripping during long-term cycling, which is an important indicator of the Li surface stability. As shown in Supplementary Figure 10, under 1 mA cm^{-2} and 1 mAh cm^{-2}, the Li‖Li symmetrical cells using the HMO-coated separators show better cycling stability than that using the bare separator. Furthermore, the cell using the HMO-5-coated separator exhibits the lowest voltage hysteresis and the most stable profile over 2000 h. These results are consistent with the performance of the Li‖Cu half cells.

Finally, the HMO-coated separators were subjected to LMB tests. The Li‖NMC811 coin cells with a high NMC811 loading of 4.3 mAh cm^{-2} were first studied. As shown in Figure 5D, radical capacity fading was reached after 50 and 100 cycles for the cells using the bare and HMO-3-coated separators, respectively, while the capacity retentions at the 200th cycle were 46.54% and 28.67% for the cells using the HMO-5 and HMO-7-coated separators, respectively. In addition, the average CE over 200 cycles was 99.85% for the cell using the HMO-5-coated separator, significantly higher than 99.67% of the HMO-7 counterpart. These results demonstrate the best Li protection ability of HMO-5 with the highest Mn^{3+}/Mn^{4+} ratio. Hence, the HMO-5-coated separator was implemented in the Li‖NMC811 pouch cell. The cell configuration is shown
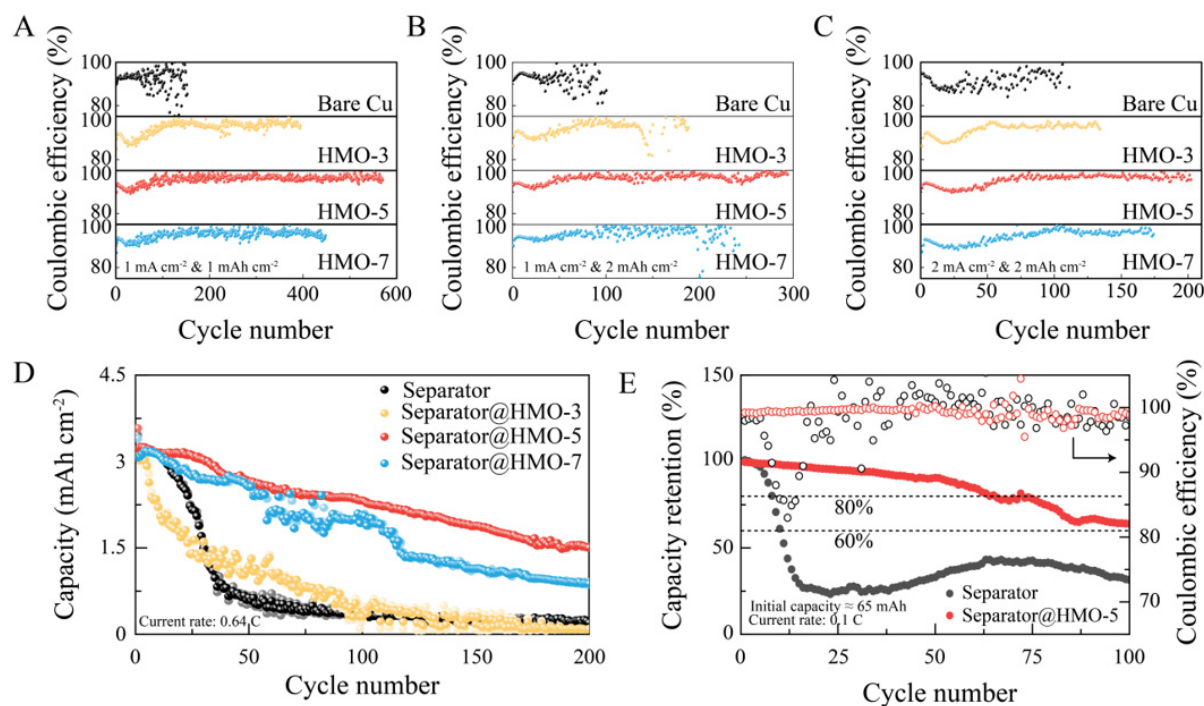
Figure 5. Li cycling CEs on investigated substrates under (A) 1 mA cm^{-2} and 1 mAh cm^{-2}, (B) 1 mA cm^{-2} and 2 mAh cm^{-2} and (C) 2 mA cm^{-2} and 2 mAh cm^{-2}. (D) cycling performances of Li||NMC811 coin cells using bare and HMO-coated separators. (E) cycling performances of Li||NMC811 pouch cells using bare and HMO-5-coated separators.

in Supplementary Figure 11 and the assembled pouch cells have an initial capacity of ~65 mAh. As shown in Figure 5E and Supplementary Figure 12, the pouch cell using the bare separator rapidly failed in less than 20 cycles. In sharp contrast, 80% capacity was retained at the 75th cycle for the pouch cell using the HMO-5-coated separator. These results demonstrate the potential applicability of this lithium adsorbent for Li protection in practical LMBs. It is noteworthy that the effect of Li protection of HMO might gradually disappear during cycles under practical conditions due to the progressive phase conversion of the metal oxides[28]. The latter issue is expected to be suppressed through the rational design of the metal oxide structure[29] and will be addressed in future studies.

CONCLUSIONS

In summary, a class of Li adsorbents has been constructed as hosts for Li metal protection, where the Mn^{3+}/Mn^{4+} ratio has been demonstrated to be a crucial factor in improving the Li plating/stripping stability. The high Mn^{3+}/Mn^{4+} ratio can afford boosted Li diffusion and adsorption kinetics, resulting in low Li nucleation and electroplating overpotentials, high Li deposition uniformity and stable Li cycling CE for both high current density and capacity. Consequently, much improved electrochemical performances have been achieved for the coin and pouch cells of Li metal batteries using the selected Li adsorbent. For the Li||NMC811 coin cell with a high NMC811 loading of 4.3 mAh cm^{-2}, a high CE of 99.85% was achieved over 200 cycles. For the Li||NMC811 pouch cell with a capacity of ~65 mAh, 80% capacity was retained at the 75th cycle, compared with the total failure of the control sample in less than 20 cycles. This work demonstrates the ability of the Mn^{3+}/Mn^{4+} tuned Li adsorbent to enable stable and dendrite-free Li metal anodes. This strategy can be applied to other metal oxides to build up a novel material base for achieving safe and high-energy Li metal batteries.

DECLARATIONS

Authors' contributions

Conceived the idea of the project: Peng Z, Yao X

Made substantial contributions to conception and design of the study and performed data analysis and interpretation and wrote the draft of manuscript: Zhao Y, Peng Z, Yao X

Performed data acquisition, as well as provided administrative, technical, and material support: Zhao Y, Liu Z, Li Z

Discussed and revised the manuscript: Zhao Y, Liu Z, Li Z, Peng Z, Yao X

Finalized the manuscript: Peng Z, Yao X

Availability of data and materials

Not applicable.

Financial support and sponsorship

Conflicts of interest

All authors declared that there are no conflicts of interest.

Ethical approval and consent to participate

Not applicable.

Consent for publication

Not applicable.

Copyright

REFERENCES

1. Chu S, Majumdar A. Opportunities and challenges for a sustainable energy future. *Nature* 2012;488:294-303. DOI PubMed
2. Choi JW, Aurbach D. Promise and reality of post-lithium-ion batteries with high energy densities. *Nat Rev Mater* 2016;1:16013. DOI
3. Liu J, Bao Z, Cui Y, et al. Pathways for practical high-energy long-cycling lithium metal batteries. *Nat Energy* 2019;4:180-6. DOI
4. Cheng XB, Zhang R, Zhao CZ, Zhang Q. Toward safe lithium metal anode in rechargeable batteries: a review. *Chem Rev* 2017;117:10403-73. DOI PubMed
5. Jiao S, Zheng J, Li Q, et al. Behavior of lithium metal anodes under various capacity utilization and high current density in lithium metal batteries. *Joule* 2018;2:110-24. DOI
6. Fan X, Chen L, Ji X, et al. Highly fluorinated interphases enable high-voltage Li-metal batteries. *Chem* 2018;4:174-85. DOI
7. Zhu C, Sun C, Li R, et al. Anion-Diluent pairing for stable high-energy Li metal batteries. *ACS Energy Lett* 2022;7:1338-47. DOI
8. Fan X, Ji X, Han F, et al. Fluorinated solid electrolyte interphase enables highly reversible solid-state Li metal battery. *Sci Adv* 2018;4:eaau9245. DOI PubMed PMC
9. Ji X, Hou S, Wang P, et al. Solid-state electrolyte design for lithium dendrite suppression. *Adv Mater* 2020;32:e2002741. DOI PubMed
10. Zhang Z, Xu X, Wang S, et al. Li_2O-reinforced Cu nanoclusters as porous structure for dendrite-free and long-lifespan lithium metal anode. *ACS Appl Mater Interfaces* 2016;8:26801-8. DOI PubMed
11. Huang S, Zhang W, Ming H, Cao G, Fan LZ, Zhang H. Chemical energy release driven lithiophilic layer on 1 m^2 commercial brass mesh toward highly stable lithium metal batteries. *Nano Lett* 2019;19:1832-7. DOI PubMed
12. Luo K, Leng Z, Li Z, et al. Shielded electric field-boosted lithiophilic Sites: a Janus interface toward stable lithium metal anodes. *Chem Eng J* 2021;416:129142. DOI
13. Peng Z, Song J, Huai L, et al. Enhanced stability of Li metal anodes by synergetic control of nucleation and the solid electrolyte interphase. *Adv Energy Mater* 2019;9:1901764. DOI
14. Zhang D, Dai A, Wu M, et al. Lithiophilic 3D porous CuZn current collector for stable lithium metal batteries. *ACS Energy Lett*

2020;5:180-6. DOI

15. Chen W, Fu M, Zhao Q, Zhou A, Huang W, Wang J. Au-modified 3D carbon cloth as a dendrite-free framework for Li metal with excellent electrochemical stability. *J Alloys Comp* 2021;871:159491. DOI

16. Zhang R, Chen XR, Chen X, et al. Lithiophilic sites in doped graphene guide uniform lithium nucleation for dendrite-free lithium metal anodes. *Angew Chem Int Ed Engl* 2017;56:7764-8. DOI PubMed

17. Wang M, Peng Z, Lin H, et al. A framework with enriched fluorinated sites for stable Li metal cycling. *Acta Physico Chimica Sinica* 2021;37:2007016. DOI

18. Kim Y, Kwon SH, Noh H, et al. Facet selectivity of Cu current collector for Li electrodeposition. *Energy Storage Mater* 2019;19:154-62. DOI

19. Gu Y, Xu HY, Zhang XG, et al. Lithiophilic faceted Cu(100) surfaces: high utilization of host surface and cavities for lithium metal anodes. *Angew Chem Int Ed Engl* 2019;58:3092-6. DOI PubMed

20. Li S, Li Z, Huai L, et al. A strongly interactive adatom/substrate interface for dendrite-free and high-rate Li metal anodes. *J Energy Chem* 2021;62:179-90. DOI

21. Julien CM, Massot M. Raman spectroscopic studies of lithium manganates with spinel structure. *J Phys Condens Matter* 2003;15:3151-62. DOI

22. Mu Y, Zhang C, Zhang W, Wang Y. Electrochemical lithium recovery from brine with high Mg2+/Li+ ratio using mesoporous λ-MnO2/LiMn2O4 modified 3D graphite felt electrodes. *Desalination* 2021;511:115112. DOI

23. Saif H, Huertas R, Pawlowski S, Crespo J, Velizarov S. Development of highly selective composite polymeric membranes for Li+/Mg2+ separation. *J Membrane Sci* 2021;620:118891. DOI

24. Zuo C, Hu Z, Qi R, et al. Double the capacity of manganese spinel for lithium-ion storage by suppression of cooperative Jahn-Teller distortion. *Adv Energy Mater* 2020;10:2000363. DOI

25. Li X, Wang Y, Wu D, Liu L, Bo S, Ceder G. Jahn-Teller assisted Na diffusion for high performance Na Ion batteries. *Chem Mater* 2016;28:6575-83. DOI

26. Pei A, Zheng G, Shi F, Li Y, Cui Y. Nanoscale nucleation and growth of electrodeposited lithium metal. *Nano Lett* 2017;17:1132-9. DOI PubMed

27. Fleischmann S, Zhang Y, Wang X, et al. Continuous transition from double-layer to Faradaic charge storage in confined electrolytes. *Nat Energy* 2022;7:222-8. DOI

28. Zhan Y, Shi P, Ma X, et al. Failure mechanism of lithiophilic sites in composite lithium metal anode under practical conditions. *Advan Energy Mater* 2022;12:2103291. DOI

29. Xu J, Sun N, Chen J, et al. Stabilizing lithiophilic sites via bimetallic oxide heterointerfaces. *Adv Mater Inter* 2022;9:2200750. DOI